Investigating the Effect of Generalized Newtonian Fluid on the Micro-Void Development within Large Scale Polymer Composite Deposition Beads

A. Awenlimobor *, D. E. Smith*, Z. Wang †,

*Department of Mechanical Engineering, School of Engineering and Computer Science, Baylor University, Waco, TX 76798, USA

†Department of Mechanical Engineering, Naval Architecture and Ocean Engineering College, Dalian Maritime University, Dalian 116000, China

Abstract

The formation and development of micro-voids within the bead microstructure of a polymer composite during the extrusion/deposition additive manufacturing process continues to be of interest given the adverse effect these features have on part quality. A computational method is employed here to investigate potential volatile-induced micro-void nucleation mechanism which simulates the evolution of a single rigid ellipsoidal fiber in purely viscous polymer extrusion/deposition flow through a Large Area Additive Manufacturing (LAAM) nozzle. Our previous studies on potential micro-void nucleation mechanisms have assumed a Newtonian fluid property definition for the polymer melt flow, the current study assesses the effect of assuming a generalized Newtonian fluid (GNF) model on the fiber's response. Preliminary findings based on Jeffery's flow assumption reveal the fiber's orientation kinetics are unaffected by the shear-thinning fluid behavior, however there is a reduction in the pressure distribution on the fiber's surface as the power law index is decreased which is expected to reduce the likelihood for micro-void nucleation.

Introduction

Investigation is currently ongoing into underlying mechanisms responsible for the formation and development of microstructural voids within parts printed from Large Area Additive Manufacturing (LAAM) process and contributory factors that may impact this phenomenon such as process parameters, fluid rheological properties, fiber fill percentage, and fibers thermomechanical properties among others.

Based on experimental studies presented in numerous literatures, various mechanisms exist that may be responsible for the nucleation and growth of these micro-voids during polymer composite processing such as uneven volume shrinkage mechanism during solidification [1,2], absorption of moisture and/or volatile contents during the bead pelletization or polymer extrusion/deposition process [2,3]. Literature suggests that the inclusion of fibers during polymer processing impact the development of these voids, for instance voids have been observed to preferentially segregate at the tip of fiber and the fiber's shape and degree of flow alignment relates to the packing density and void content and characterization [2]. Studies have also shown that these micro-voids are more likely to develop near the die swell region of the nozzle exit during bead deposition on the moving bed [4].

Modelling of the extrusion-deposition process to determine the polymer melt flow characteristics and flow-field states have employed various traditional techniques such as finite element method (FEM), smoothed particle hydrodynamics (SPH), finite-difference method (FDM*), finite-volume method (FVM), discrete element method (DEM) etc. For example, the FEM technique was utilized by Heller et al. [5], Wang et al. [6] and Russell et al. [7] among other researchers to simulate the deposition process and determine average orientation tensor response of short carbon fibers in polymer suspension flowing through a LAAM nozzle extruder in other to evaluate approximate thermo-mechanical properties. FVM technique was used by Xia et al. [8] to model coupled heat transfer and polymer flow deposition process.

Most numerical studies on particle migration in homogeneous viscous flow have been based on the assumptions of negligible inertia effects, Newtonian fluid rheology and non-deformable particle shape conventionally referred to as "standard conditions" [9]. Recent studies have focused on accounting for discrepancies in predictions of the kinematic behavior of suspended fibers theoretically having indeterminate motion when computed from analytical formulations that are based on standard conditions compared with actual experimental observations that reveals acquiescence of suspended particles to equilibrium configuration within a characteristics timescale or equilibrium rate of approach irrespective of their initial configuration due to the cumulative effect over time of small deviations from "standard conditions". Saffmann et al [10] showed that preferred configurations are not always a certainty however when they occur, of the possible effects that may be responsible for the observed deviations from theoretical predictions of particle motion, the non-linear contribution of the fluid inertial were infinitesimal as to significantly alter the motion in a finite timescale while neglected effects of the non-Newtonian viscosity accounted mainly for the observed phenomenon. Other effects such as the particles inertia, confinement and end effect were deemed negligible.

Various computational models that account for the neglected effects of non-Newtonian fluid rheology have been developed to investigate the degree of departure from theoretical predictions of fiber kinematics based on standard conditions. Ferec et al. [11] developed a two-dimensional (2D) FEM model that simulates the motion of a single ellipsoidal fiber in an unconfined non-Newtonian power law fiber suspension simple shear viscous flow to evaluate the magnitude of departure of the predicted fiber kinematics responses from results of standard theoretical model based on Newtonian fluid assumptions. His model is based on minimization of the net force and couple acting on the particle due to the surrounding fluid pressure. He found that the shear-thinning effect only slightly affected the particle's kinematic, and this impact diminishes with increasing fiber slenderness.

While there has been significant research progress in the development of accurate experimental methods and numerical models to better understand the fiber dynamics in fiber-filled viscous suspension with non-Newtonian fluid rheology during polymer processing, there has been very little effort to study the formation and growth of voids within the bead's microstructure of polymer composites materials and how the introduction of fibers interacts and influence the development of these voids. Besides the conventional 3D micro-CT-Scan techniques for investigating microstructural defects, various cost-saving, non-destructive, and non-intrusive

techniques have been developed [12, 13]. Sayah et al. [14] studied the void content, distribution, and their characterization within the microstructure of beads printed from a LAAM nozzle extruder and the relation between these void parameters and operating conditions. They observed decreased void content with increasing process temperature and print speed, and the void contents also decreased upon bead deposition. Recently, Awenlimobor et al. [15] used 2D FEM based minimization technique to study the evolution of the pressure distribution on a fibers surface in fiber suspension with Newtonian fluid rheology during the polymer/extrusion deposition process. They found that the minimum localized pressure distribution occurring at the fiber's tip dropped well below the flow pressure which indicated the likelihood for potential void nucleation at these sites for polymers with non-zero vapor pressure.

The present study is an extension to previous work by Awenlimobor et al [15]. Here, we perform FEM-based simulations to investigate the effect of a generalized Newtonian fluid (GNF) rheology on Jeffery's orbit and potential volatile-induced micro-void nucleation mechanism by simulating the single fiber motion along streamlines of a polymer extrusion/deposition flow through a LAAM nozzle. We explore the contribution of various factors such as the fibers geometric aspect ratio, and initial fiber angle in addition to the effect of the shear-thinning fluid characteristics (power-law index and consistency index) on the particles motion and responses. A multiscale methodology similar to [15,16] is employed for the investigation. Firstly, a 2D planar deposition flow macro-model that simulates the polymer composite extrusion-deposition process within a LAAM nozzle extruder is developed to compute flow-fields and streamline data which then serves as inputs to a single fiber micromodel. The micromodel development is a GNF nonlinear extension to the formulations of Zhang et al.[17,18,19], and simulates the fibers motion along streamlines obtained from the macro-model. A power-law non-Newtonian fluid model is assumed for fiber suspension rheology. Newton Raphson iteration is used to compute the resulting translational and rotational velocities of the rigid fiber particle by zeroing the net force and couple acting on the fiber. The fiber's instantaneous positions and orientations are then updated using a numerical ordinary differential equation (ODE) solution technique. FEA model validation is achieved by comparing steady state responses at a single time step of the quasi-transient analysis of a single fiber motion along Jeffery's orbit obtained from our custom-built FEA simulation with results obtained from simulations using the COMSOL Multiphysics commercial software. The resulting effect of the shear thinning fluid behavior on the evolution of the pressure distribution response on the fibers' surface as it travels along streamlines is an indication of the potential role of the fluid rheology in mitigating the micro-void nucleation in polymer suspension during processing. The results of this study strictly speaking are to be construed in a qualitative sense rather than an actual quantification analysis.

Methodology

The methodology used in the present study is analogous to that presented in [15,16] which is based on a one way coupling multiscale modelling approach to simulate the fiber-filled polymer composite bead printing process via a LAAM nozzle extrusion-deposition technology in order to better understand the development of micro-voids within the printed beads. The macro-scale model is developed to compute the flow fields and orientation tensors from the velocity solution along

streamlines of the polymer melt flow process through the LAAM nozzle. The velocity and pressure responses computed from the macro-model analysis are used to extrapolate boundary conditions in the development of the micromodel which simulates the evolution of a single rigid ellipsoidal fiber along streamlines of the macro-model. A shear-thinning power law fluid model has been assumed for both micro-model and micro-model analysis with consistency index equal to the magnitude of the average Newtonian fluid viscosity. The study is performed for 13% carbon fiber filled ABS polymer melt material with a characteristic's density of 1154 kgm³ and kinematic viscosity of $817Pa \cdot s$ averaged at 230°C and a flowrate of $100s^{-1}$.

Macro-Model: Planar Extrusion-Deposition Flow Model

The development of the 2D planar extrusion-deposition flow model of the fiber filled polymer composite material through the LAAM nozzle extruder has been provided in much details in Wang, et al [20]. The Strangpresse Model 19 LAAM single screw extruder nozzle design has been adopted for the internal nozzle geometry used in this study. The model equations describing the polymer melt flow within the LAAM nozzle and the single bead deposition on the moving bed are based on the Stokes assumption of creeping, incompressible, isothermal, steady state, low Reynolds number viscous flow and the mass and momentum conservation equations are given in Equations 1-2.

$$\underline{\nabla}^T \underline{u} = 0$$

$$\underline{\nabla}^T \underline{\underline{\sigma}} + \underline{f} = 0$$
2

In Equations 1-2, above, $\underline{\nabla}$ is the gradient operator, \underline{u} is the flow velocity vector, \underline{f} is the body force vector, and $\underline{\underline{\sigma}}$ is the Cauchy stress tensor given as :

$$\underline{\underline{\sigma}} = \underline{\underline{\tau}} - p\underline{\underline{I}}$$
 3

 $\underline{\underline{\sigma}} = \underline{\underline{\tau}} - p\underline{\underline{I}}$ In Equation 3, p is the hydrostatic fluid pressure, $\underline{\underline{I}}$ is the identity matrix, and $\underline{\underline{\tau}}$ is the deviatoric stress tensor defined in terms of the deformation tensor $\dot{\gamma}$ by the constitutive relation given as

$$\underline{\underline{\tau}} = 2\eta(\dot{\gamma})\underline{\dot{\gamma}}$$

The viscosity η in Equation 4 above is expressed in terms of an invariant of the deformations tensor $\dot{\gamma}$ by a power-law definition given as

$$\eta(\dot{\gamma}) = m\dot{\gamma}^{n-1} \tag{5}$$

where m is the consistency index, n is th flow behavior index and $\dot{\gamma}$ is the scalar magnitude of the deformation tensor $\dot{\underline{\gamma}}$ given as $\dot{\gamma} = \sqrt{\frac{1}{2} \dot{\underline{\gamma}} : \dot{\underline{\gamma}}}.$

Figure 1a is a schematic representation of the flow domains where Ω_1 represents the nozzle internal region, Ω_2 is the die swell/expansion region where the bead exits the nozzle and Ω_3 is the single bead layer of polymer composite material deposited on the laterally translating subtrate. The prescribed boundary conditions are also depicted in the figure. At the nozzle inlet Γ_1 , an average normal velocity of 24mm/s is imposed, at the nozzle inner wall lining Γ_2 , a no slip boundary condition is defined and at the unbound surfaces of the single bead deposited layer Γ_3 , a freesurface boundary condition is imposed. The single bead deposited layer translates together with the substrate with an average velocity of 101.6mm/s in the positive x-direction prescribed at the interface between the bead layer and substrate Γ_4 and at the flow exit Γ_5 .

Figure 1b shows computed streamlines obtained from the velocity solution of the macro-model analysis that form between the nozzle inlet Γ_1 and the bead flow exit Γ_5 with three (3) feature streamlines (ψ_4 , ψ_{10} , and ψ_{18}) highlighted. ANSYS Polyflow (ANSYS Inc., Canonsburg, PA, USA) was used for macro-model analysis. A shear-thinning fluid with power law index of $n \approx$ 0.45 and a consistency coefficient of $m \approx 10^4 Pa \cdot s^n$ has been used (cf. Figure 2a). As n approaches 1, the viscosity approaches the Newtonian value equal to the consistency coefficient corresponding to a shear-rate of unity. The computed streamlines and resulting velocity profile distribution across sections of the nozzle for the non-Newtonian studies in comparison to results of the Newtonian analysis [20] are presented in Figure 1b. While the velocity profiles of the Newtonian analysis are parabolic in shape, the profiles of the non-Newtonian analysis are somewhat hyperbolic shaped with a velocity plateau towards the center tending towards a plug flow velocity distribution. Figure 2b & c shows that the velocity magnitudes and shear-rates are relatively higher at the nozzle edges ($\psi_4 \& \psi_{18}$) and lower towards the centerline (ψ_{10}) for the shear-thinning fluid compared to the Newtonian fluid. Correspondingly, the deposition times are relatively shorter for streamlines closer to the nozzle edge and relatively longer for streamlines closer to the centerline for the shear-thinning fluid compared to the Newtonian fluid. Likewise, Figure 2d shows that the pressure-drop and pressure gradients across the nozzle are less severe for the shear-thinning fluid compared to the Newtonian fluid.

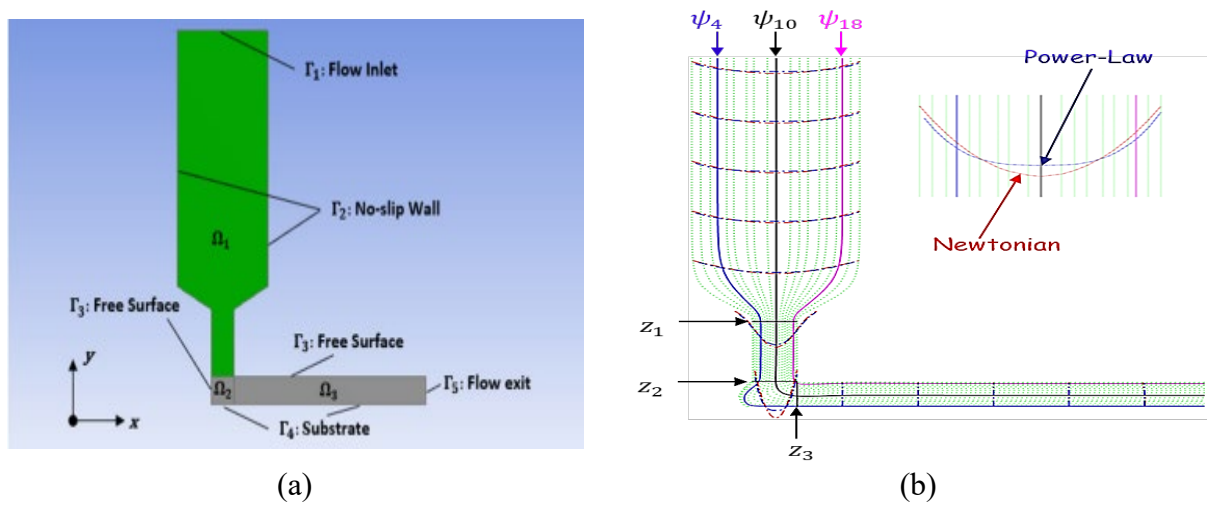


Figure 1: 2D Planar extrusion/deposition flow model a) fluid domain and boundary conditions, b) velocity streamlines of the polymer flow through the nozzle with feature streamlines highlighted.

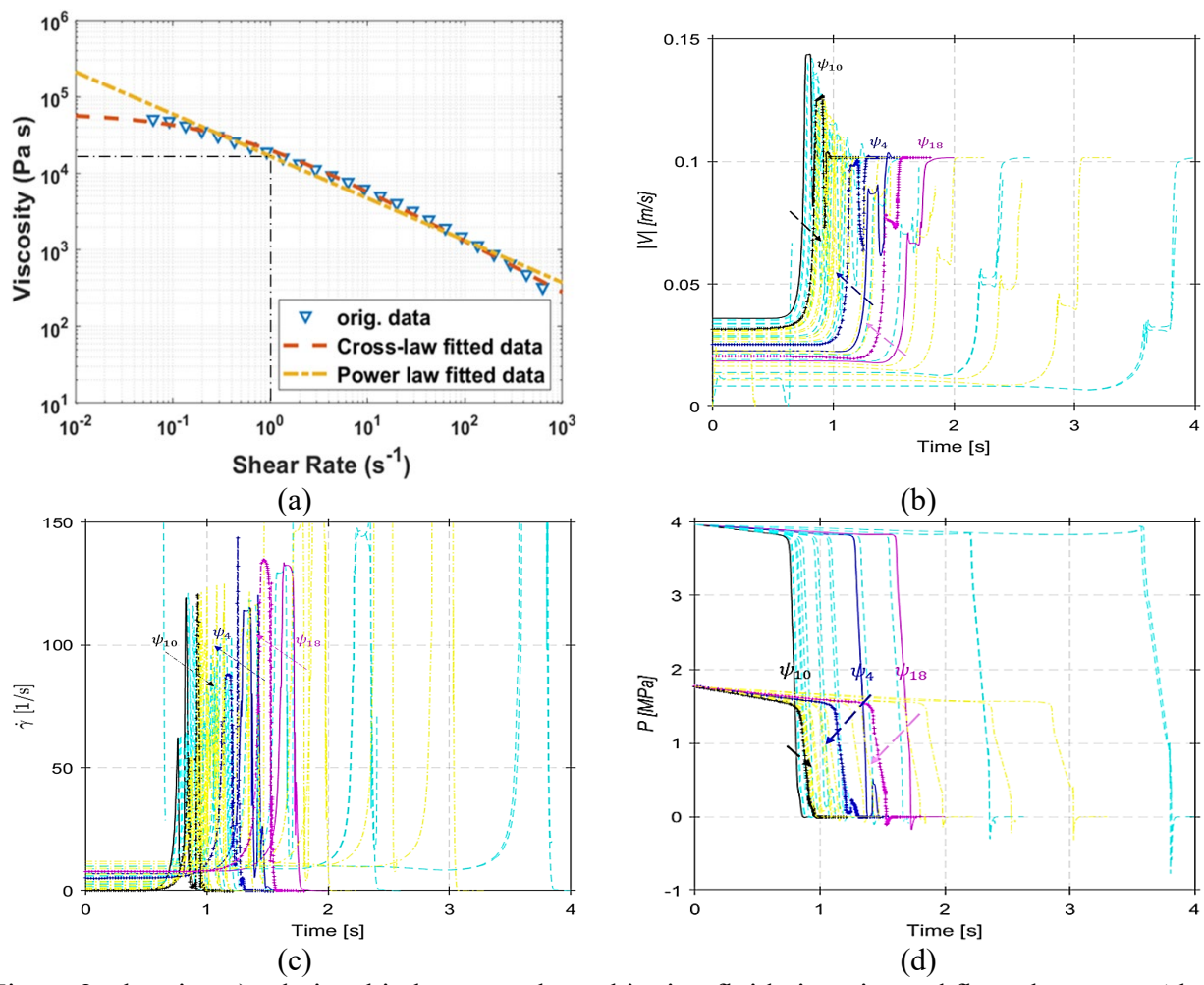


Figure 2: showing a) relationship between shear-thinning fluid viscosity and flow shear-rate. Also shown are time-varying profiles along streamline ψ_4 (blue), ψ_{10} (black) and ψ_{18} (pink) for the both Newtonian (continuous line) and non-Newtonian (dotted line) analysis results for b) velocity magnitude c) shear-rate scalar magnitude, and d) pressure distribution.

Micro-Model: 2D Single Fiber Evolution Model

In the micro-model analysis, we simulate the evolution of a single rigid ellipsoidal fiber along the streamlines of the polymer composite extrusion-deposition flow. The flow domain Ω for the single fiber evolution micromodel analysis is shown in Figure 3a. The micro-model formulations are nonlinear modifications to the model development by Zhang et. al. [17,18,19] and the governing equations are the same Stokes equations for mass and momentum conservation used in the macro-model given in Equations 1-4, based on the same assumption of isothermal, incompressible, homogenous viscous flow with a non-Newtonian power-law fluid definition. The analysis is performed with a custom-built finite element analysis (FEA) script developed in MATLAB. We assume a non-porous fiber surface with zero slip allowance. The velocity boundary conditions are prescribed with respect to the fiber's local coordinate reference axes (cf. Figure 3b). A typical schematic showing the configuration of the fibers' axis with respect to simple shear flow-field in 2D space is shown in Figure 3c.

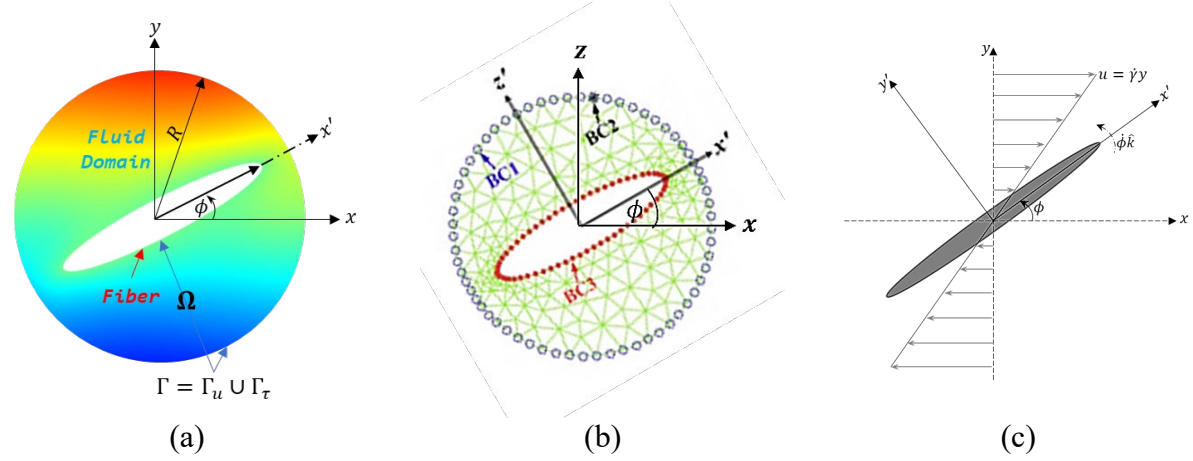


Figure 3: Micromodel showing (a) flow domain (b) prescribed boundary conditions, (c) fiber orientation with respect to flow-field.

Similar to our previous Newtonian analysis [15], the velocities and velocity gradients of the streamline data obtained from velocity solutions of the micromodel are used to derive the far-field velocities on the fluid domain boundary \underline{U}^{BC1} of the micromodel according to Equation 6 below.

$$\underline{\underline{U}}^{\text{BC1}} = \underline{\underline{R}}_{\Omega}^{T} \underline{\underline{U}}_{\psi} + \underline{\underline{R}}_{\Omega}^{T} \underline{\underline{V}}^{T} \underline{\underline{U}}_{\psi} \underline{\underline{R}}_{\Omega} \underline{\Delta} \underline{R}^{BC1}$$

$$6$$

where the streamline velocity vector \underline{U}_{ψ} , the gradient vector and the position vector $\underline{\Delta R}$ are represented in terms of their components below.

$$\underline{U}_{\psi} = \begin{bmatrix} u_{\psi} \\ v_{\psi} \end{bmatrix}, \qquad \underline{\nabla}^{T} = \begin{bmatrix} \partial/\partial x & \partial/\partial y \end{bmatrix}, \qquad \underline{\Delta}\underline{R} = \begin{bmatrix} \Delta x' \\ \Delta y' \end{bmatrix}$$

The local to global transformation matrix $\underline{\underline{R}}_{\Omega}$ is defined in terms of the in-plane fiber orientation angle ϕ and is given as

$$\underline{\underline{R}}_{\Omega} = \begin{bmatrix} \cos \phi & \sin \phi \\ -\sin \phi & \cos \phi \end{bmatrix}$$
 8

We compute the velocities on the fiber's surface \underline{U}^{BC3} from the fiber's center translational and rotational velocities based on to the equation of rigid body motion which is given with respect to the fibers local reference axis as

$$\underline{U}^{\text{BC3}} = \underline{R}_{\Omega}^{T} \underline{U}_{c} + \hat{\phi} \times \underline{\Delta} \underline{R}^{BC3}$$

where the fibers translational velocity vector is given as $\underline{U}_c = [u_c \quad v_c]^T$ and $\hat{\phi}$ is the in-plane angular velocity. A pressure point constraint p_{BC2} is imposed on a bounding node on the far-field fluid domain with a magnitude equal to the instantaneous streamline pressure p_{ψ} derived from the macro-model outputs, i.e.

$$p_{BC2} = p_{\psi} \tag{10}$$

We retain the same fluid domain discretization for the base case with fiber's geometric aspect ratio $r_e = 6$ however for the sensitivity analysis involving large fibers aspect ratio $r_e = 30$, the MATLAB inbuilt PDE modeler is used to discretize the fluid domain with increasing mesh density towards the fiber and fibers tip (cf. Figure 4a & b). A 6-node quadratic, iso-parametric triangular serendipity element shown in Figure 4c has been used for the FEA simulation.

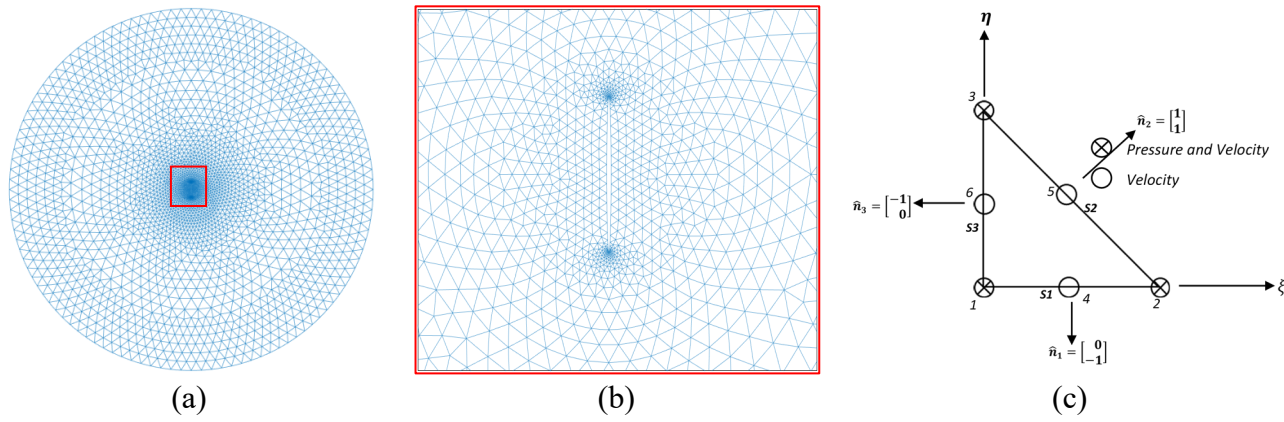


Figure 4: (a) Fluid domain discretization (b) magnified view of the domain mesh around the rigid fiber (c) element selection with active dof.

The nonlinear finite element algebraic equations are written in terms of the solution variable (u) typically represented in terms of the global system residual vector R given as:

$$\underline{R} = \underline{K}(\underline{u})\underline{u} - f$$
 11

 $\underline{R} = \underline{\underline{K}} (\underline{u})\underline{u} - \underline{f}$ where $\underline{\underline{K}}$ is the global system 'stiffness' matrix, \underline{u} is the primary variable vector containing nodal velocities and pressures degrees of freedom and f is the secondary variable vector containing the associated nodal reaction forces and flow rates. To simplify the solution procedure, the global system matrix is partitioned into essential 'e' (unknown) and free 'f' (known) degrees of freedom as.

$$\underline{R} = \left\{ \underline{\underline{R}}_{f} \right\} = \left\{ \underline{\underline{\underline{K}}}_{f} f \quad \underline{\underline{\underline{K}}}_{f} e \right\} \left\{ \underline{\underline{\underline{u}}}_{f} \right\} - \left\{ \underline{\underline{f}}_{e} + \underline{\underline{\underline{r}}}_{e} \right\}$$
12

The unknown free velocities and pressures dofs in $\underline{\overline{u}}_f$ are computed via a Newton Raphson iterative algorithm by zeroing the free residual vector \underline{R}_f . i.e $\underline{\overline{u}}_f$ is iteratively updated until it approaches the actual solution according to

$$\underline{\overline{u}}_f^+ = \underline{\overline{u}}_f^- - \underline{\underline{J}}_f^{-1}\underline{R}_f$$
 13

The Tangent Stiffness Matrix (TSM) or Jacobian J_{ff} in Equation 13 above is obtained by differentiating the free residual vector \underline{R}_f with respect to the free degrees of freedom $\underline{\overline{u}}_f$ in the usual manner folloing a procedure similar to that given in [15,16]. Details are omitted here for conciseness.

Given the initial condition of the fiber \underline{X}^{j-1} at any instant with an associated velocity $\underline{\dot{X}}^{j-1}$ at each j^{th} time step, we update fiber's position and orientation $\underline{\dot{X}}^{j}$ using on an explicit fourth order Runge-Kutta method.

Results and Discussion

Micro Model Analysis Validation

The micro model development is validated by benchmarking pressure response obtained from the custom-built MATLAB FEA simulation for a single steady state condition and fiber configuration with outputs obtained from a similar simulation developed with COMSOL Multiphysics software using same model input. A fibers geometric aspect ratio $r_e = 6$ is used for the validation exercise, and a simple shear flow field with a shear rate of $\dot{\gamma} = 1~s^{-1}$ is imposed. We consider two different power law fluid definition with different flow behavior index n, for the first case (a) n = 0.2, and for the second case (b) n = 1., both cases having a consistency coefficient $m = 1~Pa \cdot s^n$. An initial fiber configuration corresponding to an orientation $\phi_0 = -0.7762~rad$ and angular velocity of $\dot{\phi}_0 = -0.5087~rads^{-1}$ has been used for the steady state analysis which is where the first minimum pressure peak occurs on the fibers surface during its evolution along Jeffery's orbit.

The result of the pressure distribution for both cases presented in Figure 5 shows good agreement between COMSOL simulation and inbuilt MATLAB FEA simulations. We observe a maximum discrepancy in pressure limits of about 6%.

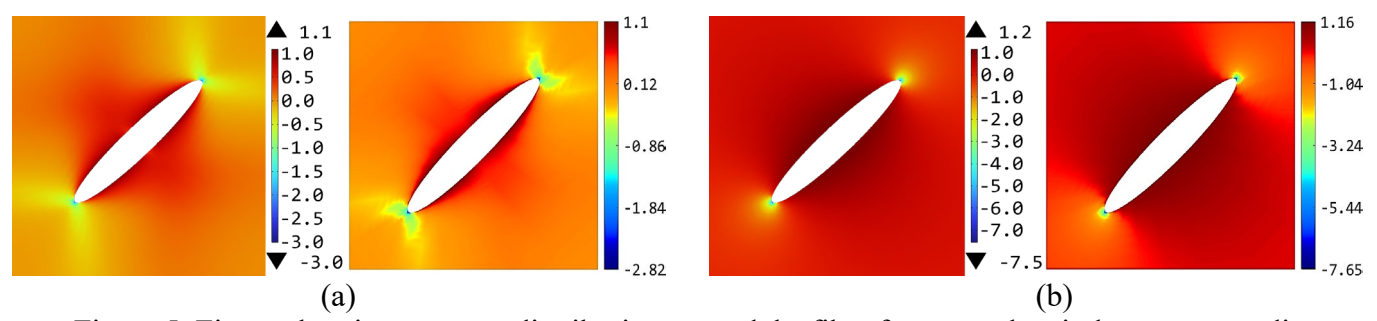


Figure 5: Figure showing pressure distribution around the fiber for power law index corresponding to (a) n = 0.2, (b) n = 1.0, for COMSOL (left of each case) and MATLAB (right of each case) simulations.

	n = 0.2		n = 1.0	
	Min	Max	Min	Max
MATLAB			-7.65	
FEA				
COMSOL	-3.01	1.10	-7.55	1.17

Table 1: Table comparing results of minimum and maximum fiber surface pressure obtained from both COMSOL and inbuilt MATLAB FEA simulations or both cases of power law indices (i.e., n = 0.2, & n = 1.0)

Single Fiber Evolution Along Jeffery's Orbit

The result for the evolution of the rigid ellipsoidal fiber along Jeffery's orbit in viscous fiber suspension simple shear flow with shear thinning fluid rheology having flow behavior index ranging from 0.2 to 1.0 are presented in Figure 6 below for two (2) cases of fibers geometric aspect ratio, i.e., a prolate spheroid with geometric ratio $r_e = 6$ and a slender fiber with geometric ratio $r_e = 30$. For the first case, a shear rate of $\dot{\gamma} = 1$ s⁻¹ is used however to reduce the orbit period for the case with high aspect, a shear rate of $\dot{\gamma} = 3$ s⁻¹ was used given the definition of the Jeffery's orbit period i.e.

$$T = \frac{2\pi}{\dot{\gamma}} \left(r_e + \frac{1}{r_e} \right) \tag{14}$$

The result in Figure 6a & b shows that irrespective of the fibers aspect ratio, the fiber's motion is unaffected by the shear-thinning fluid rheology in agreement with the findings of numerous literatures [11]. Although only a single periodic motion was computed, there was no significant effect of the shear thinning fluid rheology observed on the fiber's motion that would result in a departure from Jeffery's orbit within a finite timescale. The minimum and maximum pressure peaks on the fiber's surface were however observed to increase proportionally with the flow behavior index for both fiber aspect ratio cases (cf. Figure 6c & d).

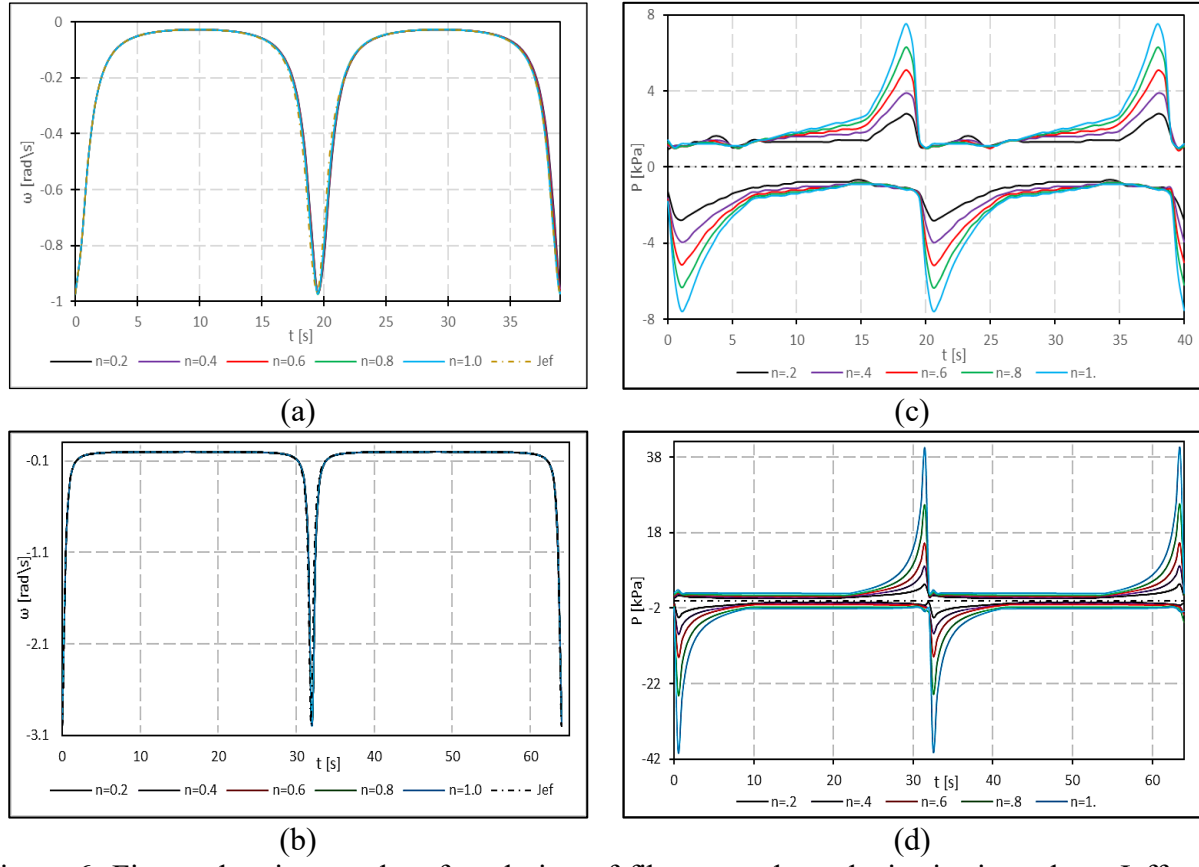


Figure 6: Figure showing results of evolution of fibers angular velocity in time along Jeffery's orbit for (a) fiber with aspect ratio $r_e = 6$, and flow with shear rate $\dot{\gamma} = 1$ s⁻¹ (b) fiber with aspect ratio $r_e = 30$, and flow with shear rate $\dot{\gamma} = 3$ s⁻¹. Also shown are results of evolution of fibers

limit surface pressure in time along Jeffery's orbit for (c) fiber with aspect ratio $r_e = 6$, and flow with shear rate $\dot{\gamma} = 1 \ s^{-1}$ (d) fiber with aspect ratio $r_e = 30$, and flow with shear rate $\dot{\gamma} = 3 \ s^{-1}$. (Results are presented for different shear-thing fluid with flow behavior index ranging from n = 0.2 - 1.0).

In Figure 7 below, we show that the fibers' initial condition does not alter the trajectory of the fiber, nor does it modify the limit pressure peaks on the fiber's surface in a shear-thinning fluid with strong non-Newtonian characteristics (flow behavior index n = 0.2).

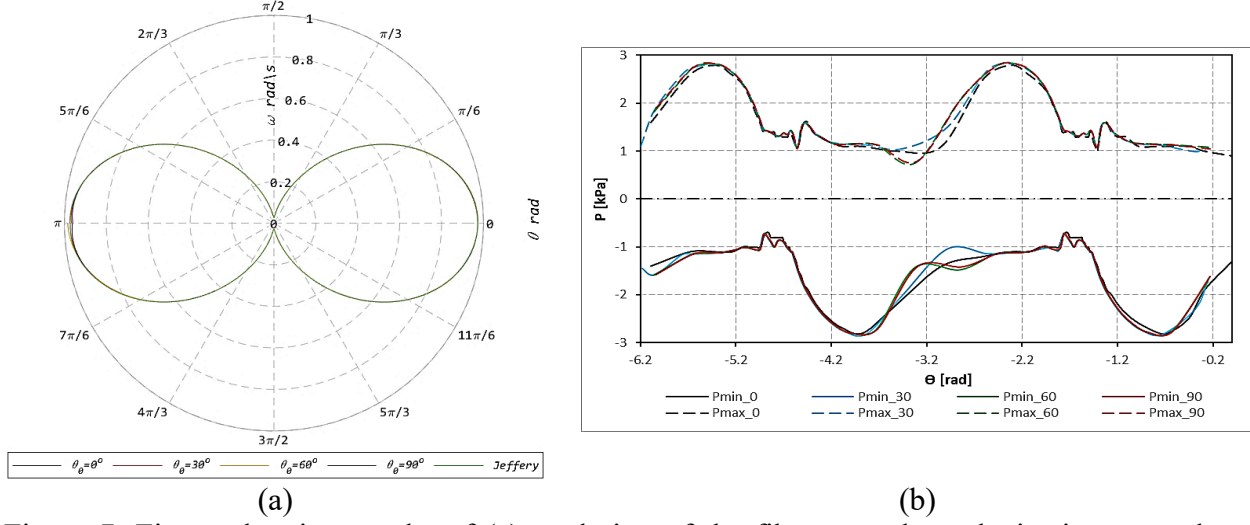


Figure 7: Figure showing results of (a) evolution of the fibers angular velocity in space along Jeffery's orbit (b) evolution of fibers limit surface pressure in space along Jeffery's orbit. Results are presented for different fiber initial orientation ($\theta_0 = 0^0, 30^0, 60^0, 90^0$) and for flow shear rate $\dot{\gamma} = 1 \, s^{-1}$, fiber aspect ratio $r_e = 6$, and flow behavior index n = 0.2.

The flow behavior index of the shear-thinning fluid has an effect analogous to the inflence of a Newtonian fluid viscosity on the pressure response on the fiber surface. Figure 8 (a) below shows the variation of the fibers surface limit pressure response with the Newtonian viscosity μ (or consistency coefficient m for power law fluid with behavior index of n=1). We see that the pressure magnitude on the fibers surface increases with increasing Newtonian viscosity similar to the influence of the flow behavior index on the pressure response. This suggests the occurrence of regions of low and high viscosities extremes on the fibers surface during the fibers tumbling motion within the non-Newtonian fluid. Figure 8 (b) shows extracted data points (blue dots) of the instantaneous shear viscosity and shear rate scalar magnitude on the fibers surface over the complete period of fiber tumbling motion and for a power law index n=0.2. The average viscosity η_1 and the viscosity corresponding to the average shear rate magnitude η_2 on the fibers surface over the entire period are also shown. From both values, η_2 is observed to be a better representation (definition) of the 'effective' mean viscosity on the fibers surface with an order of magnitude similar to the flow viscosity due to the imposed shear rate on the flowfield.

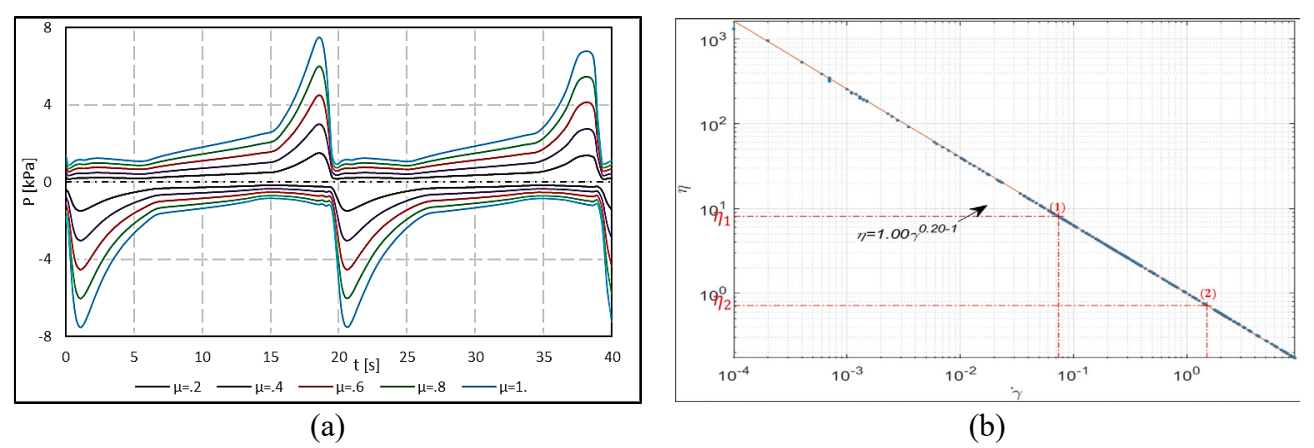
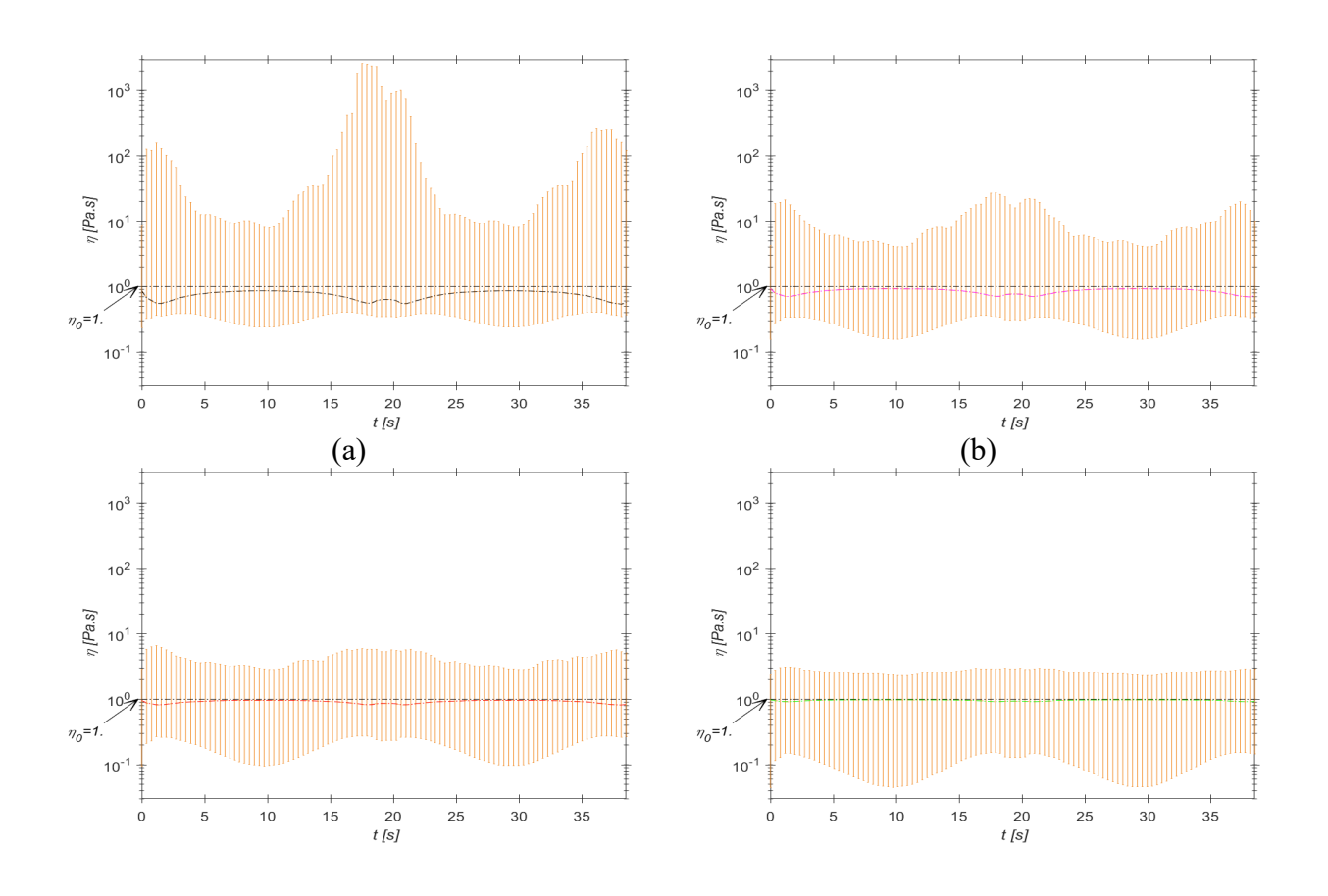


Figure 8: Figure showing (a) the evolution of fibers limit surface pressure in time along Jeffery's orbit for the Newtonian Studies and for Newtonian viscosity ranging from $\mu = 0.2 - 1.0$. (b) Scatter plot of the shear rates and resulting shear viscosities on the fibers surface over the complete period of fiber tumbling motion. Indicated on the plot are the mean value points (1 & 2) of the shear rate and viscosities.

To gain a better understanding on the dynamics of the shear viscosities on the fiber surface during its tumbling motion and its influence on the fibers surface limit pressures, we present transient profiles of the evolution of the effective mean shear viscosity η_2 and the corresponding viscosity limits at each time interval for different flow behavior index (cf. Figure 9).



(c) (d)

Figure 9¹: Figure showing time evolution of the average and limits of the non-Newtonian viscosity on the fiber's surface for different flow behavior index (a) n = 0.2, (b) n = 0.4, (c) n = 0.6, (d) n = 0.8. For the Newtonian case, all upper & lower limits of the viscosities and effective mean viscosity transient profile all coincide with the far-field viscosity at $\eta_0=1$.

From the profiles, we see that although the limits of shear rates magnitudes and resulting viscosities increases with decreasing low behavior index, the effective mean viscosity η_2 on the fibers surface only slightly shifts below the actual farfield viscosity η_0 . Following the effect of the Newtonian viscosity observed on the pressure limits on the fiber surface (cf. Figure 8(a)), we can infer in a qualitative sense that the decreasing trend in the effective mean viscosities with decreasing flow behavior index observed ovr the tumbling period in Figure 9a-d above are responsible for the low pressure limit magnitudes on the fiber surface.

Single Fiber Evolution in Extrusion-Deposition Flow

We present results of the rigid ellipsoidal fiber's motion and surface limit pressure evolution along streamlines of the extrusion-deposition flow for a single fiber suspended in a shear-thinning viscous fluid based on the micro-model non-Newtonian analysi. The results are presented for three (3) feature streamlines i.e. streamline ψ_4 closer the left edge of the nozzle, streamline ψ_{10} at the nozzle center and streamline ψ_{18} at the right edge of the nozzle (cf. Figure 2b)

Like the Jeffery studies, we see from Figure 10a-c that the fibers angular velocities are unaffected by the shear-thinning fluid rheology irrespective of the non-uniform veloity gradients that characterizes the extrusion-deposition flowfield especially at the nozzle edges and a Newtonian analysis is sufficient to predict fiber's motion. This is evident from the overlap of the angular velocity profles for all flow-behavior indices considered. On streamline ψ_4 , the fiber experiences a spin reversal upon exiting the nozzle within the region of die swell due to counterrotation in the 90° bend that opposes the local shear-vorticity direction at the left innerwall of the straight capillary before returning to steady state during bed deposition. On streamline ψ_{10} , the fiber's motion is steady within the straight capillary due to the uniform flow-field at the center streamline however the angular velocity peaks within the die-swell region due to the change in flow direction. On streamline ψ_{18} the fiber experiences two (2) significant peaks in the angular velocity along the flowpath. The first peak occurs as a result of the severe velocity gradient at the right edge of the nozzle while the latter occurs due to abrupt change in flow direction at the sharp notch where the polymer exits the nozzle. Figure 10d-e shows that the shear-thinning fluid rheology reduces the magnitude of the fibers surface pressure peaks as the flow behavior index is reduced. The implication of this is that we expect lower probability of void nucleation with higher void formation times for fiber suspension with strong shear-thinning fluid characteristics than for weakly non-Newtonian fiber suspension. The magnitude of minimum pressure drops on the fiber

 $\gamma \rightarrow \infty$ $\gamma \stackrel{\cdot}{\rightarrow}$

¹ The plots indicate viscosity limits on the fiber surface are exacerbated as the flow behavior index decreases due to the power law relationship. i.e., $\lim_{n\to 0} \eta \to 0$ and $\lim_{n\to 0} \eta \to \infty$.

surface are observed to be significantly higher on edge streamlines (ψ_4 , & ψ_{18}) compared to the center streamline (ψ_{10}). The net pressure extremes with respect to the instantaneous streamline pressure are observed to be higher at the second peak location for streamlines (ψ_4 , & ψ_{10}) except on streamline ψ_{18} where the net pressure magnitude is seen to be higher at the first peak location.

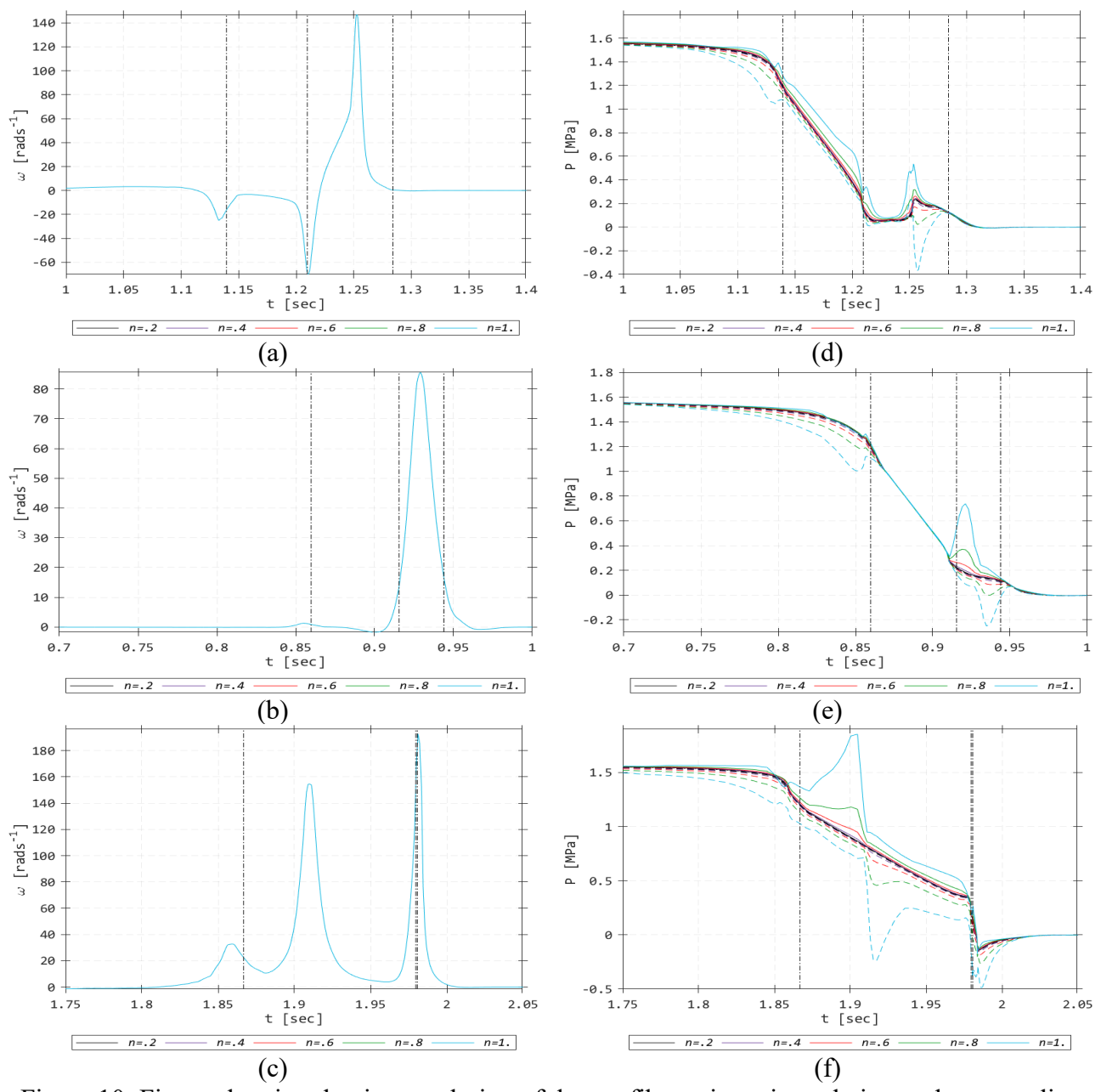


Figure 10: Figure showing the time evolution of the net fiber orientation relative to the streamline direction for (a) streamline ψ_4 , (b) streamline ψ_{10} and (c) streamline ψ_{18} . Also shown is the time evolution of the extreme pressure distribution on the fibers surface for (d) streamline ψ_4 , (e) streamline ψ_{10} and (f) streamline ψ_{18} . Results are presented for flow behavior index ranging from n = 0.2 - 1.0

Figure 11 shows that like the Newtonian case, the peak sites of minimum pressure drop are observed to occur at the fiber's tips when they do occur. Moreover, the deposition times at which the peak pressure magnitudes occur are only slightly modified by the shear-thinning fiber suspension. For the edge streamlines at the second peak location of minimum pressure drop, the time of occurrence are slightly shifted downstream the extrusion-deposition flow while for the center streamline, the time of occurrence is slightly shifted upstream the flow. As such the orientation angle at which the second peak minimum pressure drop on the fibers surface occurs is slightly modified.

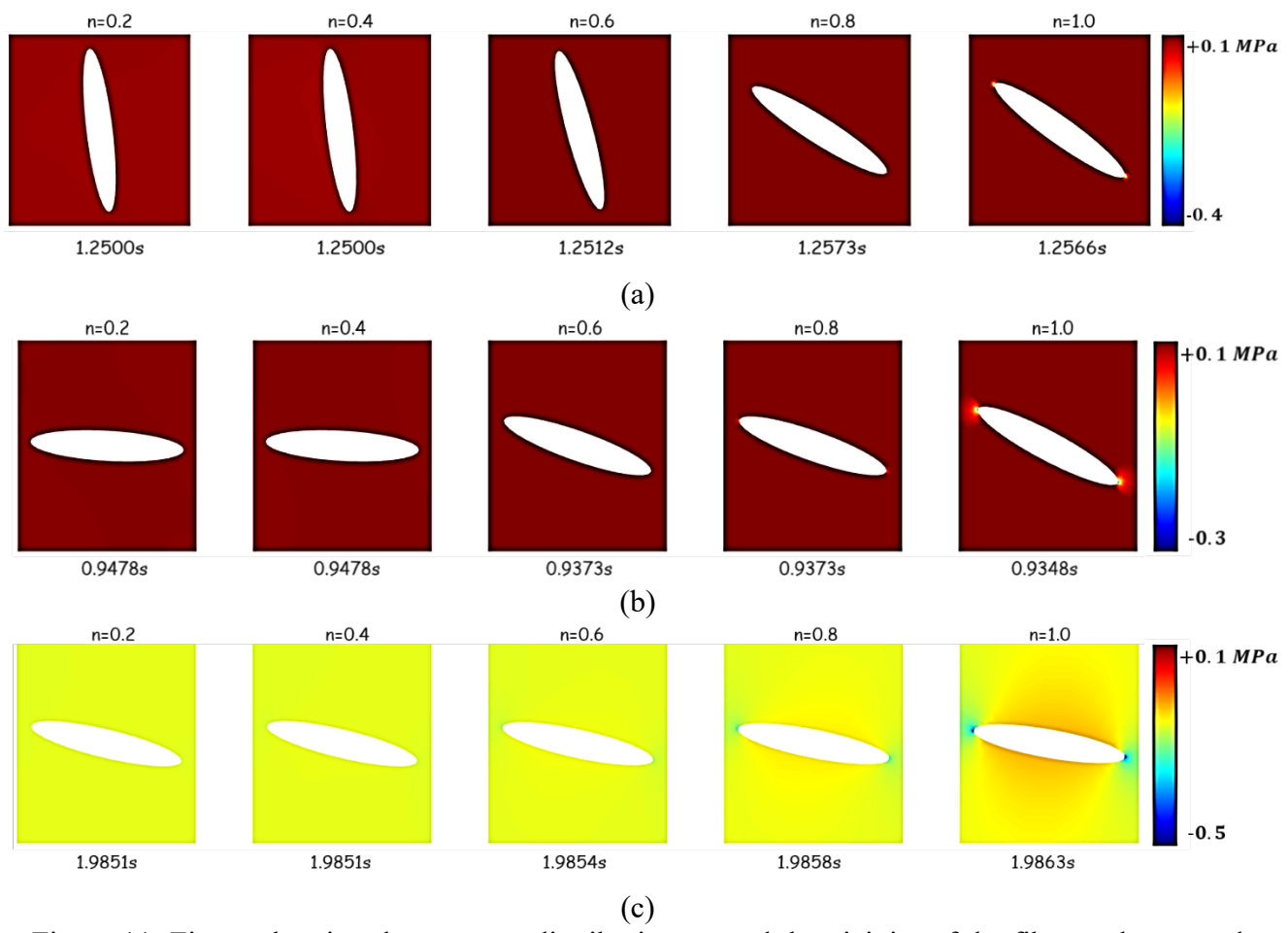


Figure 11: Figure showing the pressure distribution around the vicinity of the fiber at the second peak location of minimum pressure drop on the fibers surface for different flow behavior index ranging from n = 0.2 - 1.0 and (a) streamline ψ_4 , (b) streamline ψ_{10} and (c) streamline ψ_{18} .

Conclusion

This paper presents a non-linear 2D FEM-based multiscale modelling approach to investigate the effect of a shear-thinning rheology on potential volatile-induced micro-void development within beads printed from LAAM extrusion-deposition process. Our findings reveal that 2D fiber motion is unaffected by the shear-thinning rheology for a fiber in unconfined viscous suspension flow irrespective of the fibers shape or initial conditions agreeing with the conclusion

of Férec et al [11]. The only non-linear contribution of the shear-thinning fiber suspension rheology on the fiber's response is a reduction in the fiber's surface pressure extremes which decreases as the power-law index decreases. Based on the classical nucleation theory, we expect lower probability of void nucleation and higher void formation times for strongly non-Newtonian fiber suspension and vice versa. The non-uniform velocity gradient that characterizes the LAAM nozzle extrusion-deposition flow does not influence the observed effect of the shear-thinning fluid rheology on the fiber dynamics or fiber responses and the peak sites of minimum pressure drop occurs at the fiber's tips similar to previous Newtonian studies [15,16]. However, the time interval and corresponding fiber orientation angle at which the peak pressure magnitudes occur are slightly modified in the shear-thinning simulations. Our findings provide insight into potential micro-void mitigation strategies that could exploit the fluid rheological behavior to improve component part quality. In future revisions, a 3D extension to the current 2D non-Newtonian fiber suspension studies would be carried out.

References

- 1. Eom Y, Boogh L, Michaud V, Sunderland P, Månson JA. Stress-initiated void formation during cure of a three-dimensionally constrained thermoset resin. Polymer Engineering & Science. 2001 Mar;41(3):492-503.
- 2. Vaxman, A., Narkis, M., Siegmann, A. and Kenig, S., 1989. Void formation in short-fiber thermoplastic composites. Polymer composites, 10(6), pp.449-453.
- 3. Roychowdhury, S., Gillespie Jr, J.W. and Advani, S.G., 2001. Volatile-induced void formation in amorphous thermoplastic polymeric materials: I. Modeling and parametric studies. *Journal of composite materials*, 35(4), pp.340-366.
- 4. Yang, D., Zhang, H., Wu, J. and McCarthy, E.D., 2021. Fibre flow and void formation in 3D printing of short-fibre reinforced thermoplastic composites: An experimental benchmark exercise. Additive Manufacturing, 37, p.101686.
- 5. Heller, B.P., Smith, D.E. and Jack, D.A., 2019. Planar deposition flow modeling of fiber filled composites in large area additive manufacturing. Additive Manufacturing, 25, pp.227-238.
- 6. Wang, Z., 2019. Computational Modeling of Fiber Reinforced Composites Melt Flow in Nozzle Extrudate for Polymer Deposition Additive Manufacturing (Doctoral dissertation, Baylor University).
- 7. Russell, T., Heller, B., Jack, D.A. and Smith, D.E., 2018. Prediction of the fiber orientation state and the resulting structural and thermal properties of fiber reinforced additive manufactured composites fabricated using the big area additive manufacturing process. Journal of Composites Science, 2(2), p.26.
- 8. Xia, H., Lu, J., Dabiri, S. and Tryggvason, G., 2018. Fully resolved numerical simulations of fused deposition modeling. Part I: fluid flow. Rapid Prototyping Journal.
- 9. Leal, L.G., 1980. Particle motions in a viscous fluid. Annual Review of Fluid Mechanics, 12(1), pp.435-476.
- 10. Saffman, P.G., 1956. On the motion of small spheroidal particles in a viscous liquid. Journal of Fluid Mechanics, 1(5), pp.540-553.

- 11. Férec, J., Ausias, G. and Natale, G., 2018, May. Numerical evaluation of a single ellipsoid motion in Newtonian and power-law fluids. In AIP Conference Proceedings (Vol. 1960, No. 1, p. 020006). AIP Publishing LLC.
- 12. Idolor, O., Guha, R.D., Berkowitz, K., Geiger, C., Davenport, M. and Grace, L., 2021. Polymer-water interactions and damage detection in polymer matrix composites. Composites Part B: Engineering, 211, p.108637.
- 13. Idolor, O., Berkowitz, K., Guha, R.D. and Grace, L., 2022. Nondestructive examination of polymer composites by analysis of polymer-water interactions and damage-dependent hysteresis. Composite Structures, 287, p.115377.
- 14. Sayah, N. and Smith, D.E., 2022. Effect of Process Parameters on Void Distribution, Volume Fraction, and Sphericity within the Bead Microstructure of Large-Area Additive Manufacturing Polymer Composites. Polymers, 14(23), p.5107.
- 15. Awenlimobor, A., Wang, Z. and Smith, D.E., 2021. Physical Modeling: Simulation of Micro-Void Development within Large Scale Polymer Composite Deposition Beads. In 2021 International Solid Freeform Fabrication Symposium. University of Texas at Austin.
- 16. Awenlimobor, A., Smith, D.E., Wang, Z. and Luo, C., 2022. Three-dimensional (3D) Simulation of Micro-Void Development within Large Scale Polymer Composite Deposition Beads. In 2022 International Solid Freeform Fabrication Symposium.
- 17. Zhang, D., 2013. Flow-Induced Micro-and Nano-Fiber Suspensions in Short-Fiber Reinforced Composite Materials Processing. University of Missouri-Columbia.
- 18. Zhang, D. and Smith, D.E., 2015. Finite element-based brownian dynamics simulation of nanofiber suspensions using Monte Carlo Method. Journal of Micro and Nano-Manufacturing, 3(4).
- 19. Zhang, D. and Smith, D.E., 2016. Dynamic simulation of discrete fiber motion in fiber-reinforced composite materials processing. Journal of Composite Materials, 50(10), pp.1301-1319.
- 20. Wang, Z. and Smith, D.E., 2021. A Fully Coupled Simulation of Planar Deposition Flow and Fiber Orientation in Polymer Composites Additive Manufacturing. Materials, 14(10), p.2596.